Periodica Polytechnica
Mechanical Engineering

Analytical and Numerical Solutions of the Rotor Flow in Tesla Turbines

61(1), pp. 12-22, 2017
DOI: 10.3311/PPme.9000

Constantin Schosser[1*], Stefan Lecheler[1], Michael Pfitzner[2]

RESEARCH ARTICLE

Received 10 January 2016; accepted after revision 27 October 2016

Abstract

This paper summarises the numerical and theoretical studies of the incompressible, laminar airflow through a single flow passage of a blade-less radial turbine. Furthermore, it yields the numerical validation of the simplified theoretical model for incompressible rotor flows without the consideration of mechanical losses. It exposes the accuracy of the simplified, analytical performance prediction and flow field for a given geometry, which is based on an optimisation of performance by solving the simplified and incompressible Navier-Stokes-Equations in cylindrical coordinates. The influences of the dimensionless machine parameters on performance and efficiency are obtained from a theoretical analysis. The stream-lines of the bulk flow are derived by analytical means. The inflow conditions for maximum performance and efficiency are theoretically determined and later compared to laminar CFD. In order to quantify the error of the simplified theoretical analysis, different inflow conditions and their influences on shaft power and flow behavior are examined by means of CFD. The development of the axial velocity distribution at the inlet zone is compared to the one from the theoretical inflow assumption. The influences of Reynolds number and revolution speed on the velocity profiles are investigated. In addition to that, a compressible flow model is introduced. Numerical results are obtained and compared to the incompressible solution. Moreover, compressibility effects on turbine performance are derived.

Keywords

laminar, incompressible, flow model, streamlines, Tesla turbine, CFD, optimisation

[1] Department of Technical Thermodynamics MB 5.1,
Faculty of Mechanical Engineering, Bundeswehr University, Munich
G-85577 Neubiberg, Werner-Heisenberg-Weg 31, Germany

[2] Department of Thermodynamics LRT 10, Faculty of Aerospace Engineering, Bundeswehr University, Munich,
G-85577 Neubiberg, Werner-Heisenberg-Weg 31, Germany

[*] Corresponding author, e-mail: constantin.schosser@unibw.de

1 Introduction

Tesla friction turbines were invented by the famous scientist Nikola Tesla [2] at the beginning of the 20th century. They are characterised by their particularly simple and blade-less rotor design and consist of several circular, parallel, flat disks with a central passage in the centre of rotation.

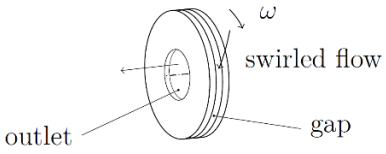

Fig. 1 Principle of energy conversion in Tesla friction turbines

All disks are equally spaced with narrow gaps. Basically any fluid is able to feed this type of turbomachine without limitations. The flow enters the gap at the outer radius of the disks under a certain inlet angle. Driven by a pressure difference, the swirling flow delivered from nozzles or guide vanes follows its spiral path to the rotor outlet at the inner disk radius. Circumferential shear stress induces torque and power. Dependent on fluid, flow parameters and geometry, Tesla turbines are able to work efficiently [3]. Their main advantages are the low-cost design, robustness and competitiveness for small scale turbomachinery, which has recently been discovered by researchers [4, 5]. Renewable and sustainable energy is the main scope of application.

After Tesla's approaches to make his turbine commercially available, the interest in his invention began in the 1950th. Theoretical and experimental research was performed, such as Rice [6]. Around the turn of the millennium, first CFD approaches came up. Currently, it is still an ongoing topic [7, 8]. Some researchers also deal with microscale friction turbines, such as Romanin et al. [4] or Krishnan et al. [5].

This paper focuses onto the flow phenomena and momentum transport inside this turbine. Laminar flow is expected for Re numbers below 300, which is typical for Tesla turbine operations (cf. Romanin et al. [9]). The study constitutes a further development of the paper of Schosser et al. [10]. The rotor dimensions

are based on the evaluation of the theoretical model for incompressible rotor flows [1]. Furthermore, it is the mechanical design of an existing test rig, which is built for the determination of the inter-disk velocity distribution inside a Tesla rotor. The velocity profiles are measured by means of particle imaging and tracking. The test facility and the demonstration of the measurement method can be found in Schosser et al. [1, 11].

2 Theoretical flow model analysis

The radial and tangential velocity distributions between co-rotating, parallel disks are illustrated in Fig. 2.

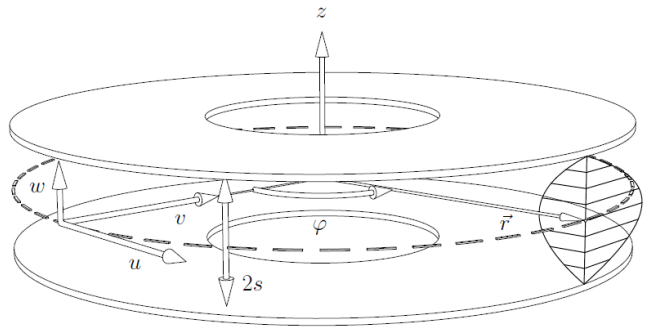

Fig. 2 Rotor flow decomposed into cylindrical coordinates

2.1 Incompressible, laminar flow description

From the semi-infinitesimal control volume, shown in Fig. 3, the governing equations for the incompressible, laminar rotor flow, which is averaged over the inter-disk spacing can be obtained. The absolute reference frame is used in here.

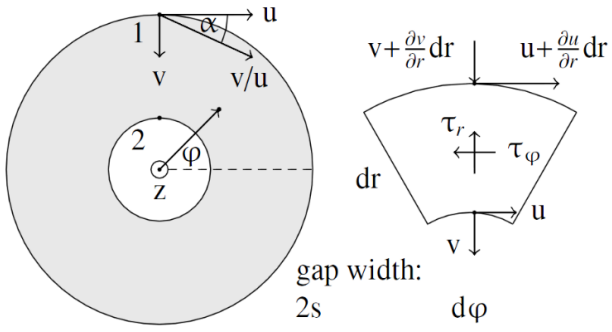

Fig. 3 Semi-infinitesimal control volume (integrated over the gap width)

In order to compute the tangential shear stress, the absolute coordinates are transformed to a relative frame by using the following expression.

$$u = c + \omega \cdot r, \tag{1}$$

The steady-state continuity equation, the tangential (φ-) and radial (r-) momentum equations for the bulk flow [1, 12, 13] can be written as

$$\frac{d(\rho \cdot r \cdot v)}{dr} = 0, \tag{2}$$

$$\rho \cdot v \cdot \left[\frac{du}{dr} + \frac{u(r)}{r}\right] - \frac{\mu}{s}\left(\frac{dc}{dz}\right) = 0, \tag{3}$$

and

$$\rho \cdot \left[v(r) \cdot \frac{dv}{dr} + \frac{u(r)^2}{r}\right] + \frac{dp}{dr} - \frac{\mu}{s}\left(\frac{dv}{dz}\right) = 0, \tag{4}$$

Equation (1) and (2) are non-dimensionalised using the following algebraic expressions

$$C(R) = \frac{c(r)}{u_1},\ U(R) = \frac{u(r)}{u_1},\ V(R) = \frac{v(r)}{u_1} \tag{5}$$

the dimensionless pressure

$$P(R) = \frac{p(r)}{\rho \cdot u_1^2} \tag{6}$$

and the dimensionless machine parameters, which are already introduced by Beans [12, 13] and recently presented in [1].

$$\beta = \frac{3}{2} \cdot \frac{r_1}{s} \cdot \frac{\nu}{v_1 s} = \frac{3}{2} \cdot \frac{r_1}{s} \cdot \frac{1}{\mathrm{Re}} \tag{7}$$

$$V_1 = \frac{v_1}{u_1},\quad \Omega = \frac{\omega \cdot r_1}{u_1},\quad R = \frac{r}{r_1} \tag{8}$$

The dimensionless governing equations result in the dimensionless tangential momentum equation in the absolute frame

$$\frac{dU(R)}{dR} + \left(\frac{1}{R} - 2\beta R\right) \cdot U(R) + 2\beta\Omega R^2 = 0 \tag{9}$$

or with the circumferential disk velocity

$$U(R) = C(R) + \Omega \cdot R \tag{10}$$

in the relative frame

$$\frac{dC(R)}{dR} + \left(\frac{1}{R} - 2\beta R\right) \cdot C(R) + 2\Omega = 0 \tag{11}$$

and the dimensionless radial momentum equation

$$\frac{dP}{dR} - V_1^2 \cdot \left(\frac{1}{R^3} + \frac{2\beta}{R}\right) - \frac{U(R)^2}{R} = 0, \tag{12}$$

For the evaluation and comparison of theoretical and CFD results, the following coefficients are defined.

$$C_{to} = \frac{A_1 v_1 \rho_1 \cdot (u_1 r_1 - u_2 r_2)}{M_{max}}, \tag{13}$$

The power coefficient is shaft power normalised with the maximum occurring power.

$$C_{po} = \frac{M \cdot \omega}{P_{max}}. \tag{14}$$

A good indicator for optimum performance is another definition of shaft power.

$$C_{pt} = \frac{P_{shaft}}{A_1 \cdot \left(p_{1,t} - p_2\right)^{\frac{3}{2}}}, \tag{15}$$

As a result of a typing error in [10], the total isentropic rotor efficiency for the incompressible flow has to be corrected and is therefrom given by

$$\eta_{is} = \frac{P_{shaft}}{\dot{m}\left[\left(\frac{p_2}{\rho} + \frac{u_2^2}{2} + \frac{v_2^2}{2}\right) - \left(\frac{p_1}{\rho} + \frac{u_1^2}{2} + \frac{v_1^2}{2}\right)\right]}. \tag{16}$$

The fully analytical solutions of Eq. (9) and (12) are already published in Schosser et al. [1]. Beginning with a two-dimensional velocity distribution across the rotor radius, the momentum transfer between wall and fluid is not yet describable. Therefore, torque and power are only obtainable with an additional assumption. This is done by assuming parabolic velocity profiles between the disks for laminar flow. The resulting wall shear stress in circumferential direction integrated over the radius leads to the performance map. The assumed profiles scale with the prevailing bulk velocities in radial and circumferential direction. Development effects of the flow at the rotor inlet are neglected in this flow model. Parameter β describes the flow rate and determines the type of vortex in the gap and is therefore crucial for the generated performance. Other important parameters for optimum performance are the inlet velocity angle V_1 (or α), the radius ratio R and the angular speed Ω, as well as the real axial velocity distribution, which are investigated and validated with CFD.

2.2 Extension to compressible, laminar flow

Based on the assumption of the incompressible model for laminar flow, the momentum equations are extended to compressible flow conditions. The energy equation is additionally required in this case. Due to the change of density, the continuity equation is then written as

$$\rho(r) \cdot r \cdot v = \rho_1 \cdot r_1 \cdot v_1. \tag{17}$$

The tangential momentum equation is then defined as

$$\rho(r) \cdot v(r) \cdot \left[\frac{du}{dr} + \frac{u(r)}{r}\right] - \frac{\mu}{s}\left(\frac{dc}{dz}\right) = 0. \tag{18}$$

The radial momentum equation is given by

$$\rho(r) \cdot \left[v(r) \cdot \frac{dv}{dr} + \frac{u(r)^2}{r}\right] + \frac{dp}{dr} - \frac{\mu}{s}\left(\frac{dv}{dz}\right) = 0. \tag{19}$$

The energy equation in an algebraic definition is

$$\dot{m}\left(u(r)r - u_1 r_1\right)\omega + \dot{m}\left[c_p\left(T(r) - T_1\right) + \frac{1}{2}\left[\left(u(r)^2 - u_1^2\right) + \left(v(r)^2 - v_1^2\right)\right]\right] = 0. \tag{20}$$

For the definition of the dimensionless governing equations, following relationships are used. The non-dimensional temperature is

$$T^*(R) = \frac{T(r)}{T_1}. \tag{21}$$

The dimensionless enthalpy is

$$H_1 = \frac{u_1^2}{c_p \cdot T_1}. \tag{22}$$

Inserting the continuity equation (19) into the perfect gas equation leads to the non-dimensional density expression

$$P_\rho(R) = \frac{\rho(r,T)}{\rho_1} = \frac{V_1}{R \cdot V(R)}. \tag{23}$$

For the expression of the dimensionless dynamic viscosity, the Sutherland formula together with Eq. (21) is used.

$$M_\mu(R) = \frac{\mu(r,T)}{\mu_1} = \frac{\mu_0}{\mu_1} \cdot \frac{T_0 + C_0}{T^*(R) \cdot T_1 + C_0} \cdot \left(\frac{T^*(R) \cdot T_1}{T_0}\right)^{\frac{3}{2}} \tag{24}$$

Using Eq. (5) to (8) and Eq. (21) to (24), the governing equations can be formulated in a non-dimensional description. The dimensionless tangential momentum equation is

$$\frac{dU}{dR} + R\left(U(R) + 2\beta M_\mu(R)\left(\Omega - U(R)\right)\right) = 0. \tag{25}$$

The radial momentum equation in a dimensionless form is

$$\frac{dP}{dR} - V_1\left(\frac{dV}{dR} + \frac{U(R)^2}{V(R)R^2} + 2\beta M_\mu(R)V(R)\right) = 0. \tag{26}$$

The energy equation is thereby defined as

$$T^*(R) = \frac{H_1}{2}\left(\frac{\Omega}{2}\left(1 - R \cdot U(R)\right) - U(R)^2 - V(R)^2 + V_1^2 + 1\right) + 1. \tag{27}$$

The differential equations are coupled solvable for certain fluid properties and initial conditions. For this numerical calculation Wolfram Mathematica or MATLAB can be used within a short computation time. The model allows the exploration of the compressibility effects of Tesla rotor flows. This is shown in Section 3.6.

2.3 Mechanical constraints

A drilled disk under constant rotation (without acceleration), generates tangential and radial mechanical stress, as illustrated in Fig. 4.

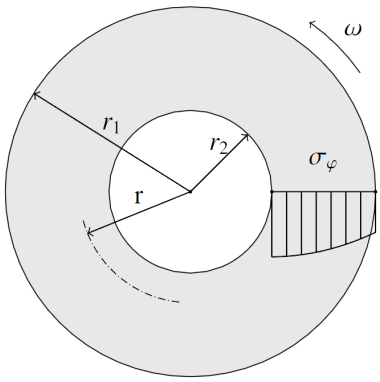

Fig. 4 Centrally drilled disk under constant rotation

The stress maximum is at the inner radius r_2 [14]. Comparing this value from Eq. (17) with the yield strength of the disk material, determines the maximum angular velocity before the disks are destroyed.

$$\sigma_\varphi\left(r=r_2\right)=\frac{3+\nu_p}{8}\rho\omega^2 r_1^2\left[1+\left(\frac{r_2}{r_1}\right)^2+\left(\frac{r_1}{r}\right)^2-\frac{1+3\nu_p}{3+\nu_p}\left(\frac{r}{r_1}\right)^2\right], \tag{28}$$

The maximum applicable angular velocity is clearly a function of the inner radius r_2, which limits the entire rev speed range of a Tesla turbine, as shown in Fig. 5. Therefore, Eq. (17) is solved for ω and made dimensionless with Eq. (8). The maximum angular velocity limit is decreasing with increasing radius ratio R (or higher inner radius rotor r_2). The analytical mechanical stress calculation consumes low computational power and offers advantages during the design process. A disk geometry for optimum flow condition is not necessarily reasonable in terms of mechanical design. This can now be judged immediately. The mechanical limitations are considered in the following model analysis and CFD.

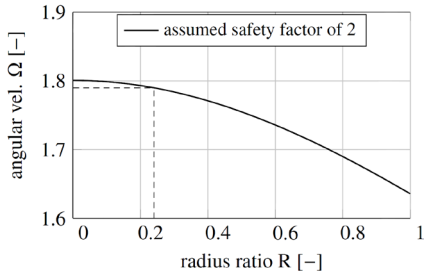

Fig. 5 Angular velocity limitations

3 Turbine model analysis

The performance map of a Tesla turbine is exemplarily shown in Fig. 6. Shaft power C_{po} is quadratic function of the angular velocity Ω, which increases with increasing values of β.

The influence of the introduced design parameters of a Tesla rotor are presented in the following sections. The results are derived from the theoretical analysis. They offer the technical limitations of blade-less rotors. To simplify illustrations, Ω is normalised by $u_1 = 100$ m/s.

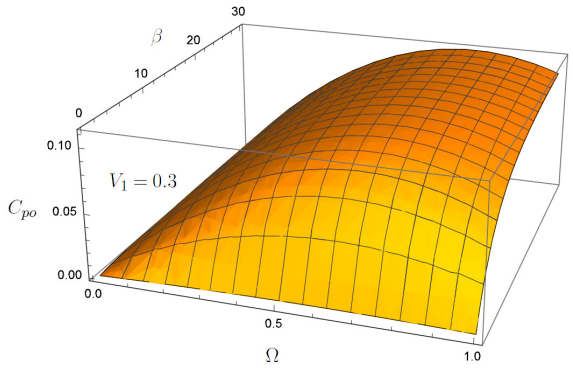

Fig. 6 Performance map of a Tesla turbine with $R = 0.8$

3.1 Dimensionless friction parameter

Schosser et al. [1] showed, that β should exceed values above ten for a performance maximum. In this case, torque and shaft power are independent of β itself. This is shown in Fig. 6 and 7.

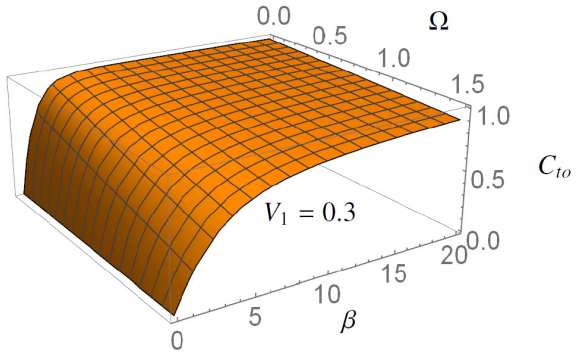

Fig. 7 Torque coefficient map of a Tesla turbine with $V_1 = 0.3$

Torque is linearly decreasing with increasing angular velocity. The torque, converted from the kinetic energy of the flow is significantly higher, if β is not too low. As β increases with decreasing gap width, the mass flow per gap is restricted. Consequently, more gaps are needed for the same magnitude of power, which increases the price of a Tesla rotor. The selection of the friction factor β is an economical decision. As a result, an upper limit of β-values between 20 to 30 is suggested.

3.2 Dimensionless inlet conditions

Tesla rotors can either be efficient or powerful. The lower V_1, the higher is the isentropic efficiency. On the other hand, a low V_1 and radial mass flow leads to low shaft power per gap. Figures 8 and 9 show normalised shaft power and efficiency as a function of angular speed. The inlet velocity magnitude is kept constant, their velocity components instead are systematically varied. This leads to a change of β and influences power and efficiency. Low V_1 corresponds to high β.

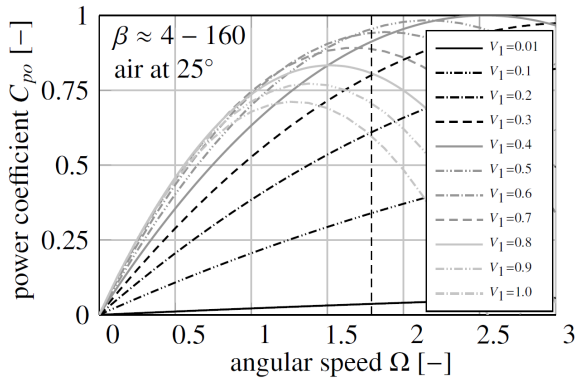

Fig. 8 Influence of the inlet angle on performance (vertical dashed line represents the mechanical limit)

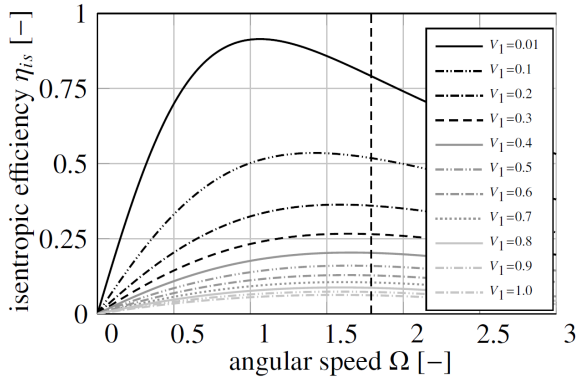

Fig. 9 Influence of the inlet angle on isentropic efficiency (vertical dashed line represents the mechanical limit)

3.3 Dimensionless geometry parameter

The most important geometry parameter for optimum performance is the radius ratio R. The influence of the radius ratio R is similar to those of the inlet angle V_1 (see Fig. 10 and 11). Low radius ratios R lead to high shaft power per gap. With increasing inner radius R_2, the area of the disks inside the turbine's gap, as well as the pressure drop across the rotor is reduced. Low pressure drops lead to highest efficiencies. In this investigation, β and V_1 are constant, the radius ratio R is altered. It is of special denote that higher radius ratios, lower the maxi-mum applicable angular speed in terms of mechanical design.

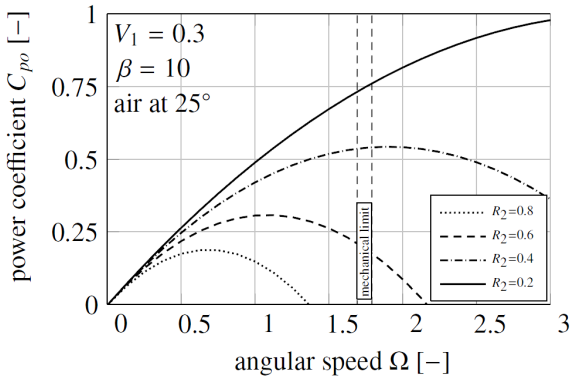

Fig. 10 Influence of the radius ratio R on performance

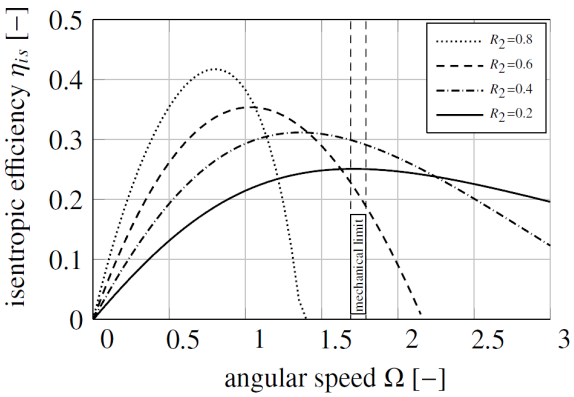

Fig. 11 Influence of the radius ratio R on efficiency

3.4 Machine parameter relations

The power coefficient C_{pt}, defined in Eq. (15) relates shaft power to the total pressure difference between inlet and outlet. When C_{pt} is at its maximum, the best compromise between power per gap and efficiency is found. Figure 12 introduces the power mapping of a Tesla rotor in terms of machine parameters Ω and R for constant and best possible values for inlet velocity ratio V_1 and friction parameter β. Optimum performance is found for $\beta > 10$, $\Omega = 0.6$, high radius ratios $R = 0.8$ and $V_1 = 0.3$.

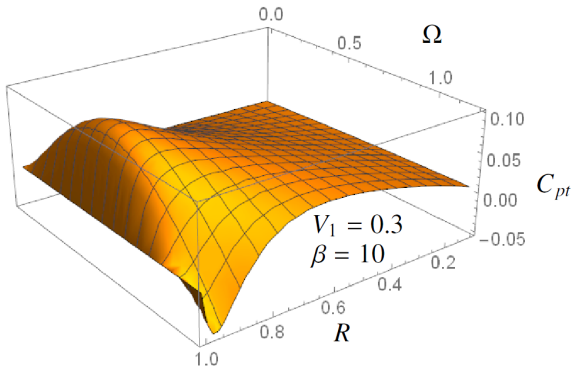

Fig. 12 Mapping of the power coefficient C_{pt}

3.5 Streamline visualisation

In an initial approximation, it is sufficient to calculate the streamlines of the incompressible bulk flow through the rotor. It can be obtained analytically by solving Eq. (18) with the boundary condition $\varphi(1) = 0$. Figure 13 shows the streamlines for different frictional conditions in the absolute reference frame.

$$\frac{d\varphi}{dR} = -\frac{U(R)}{V_1} - \frac{\varphi}{R} \tag{29}$$

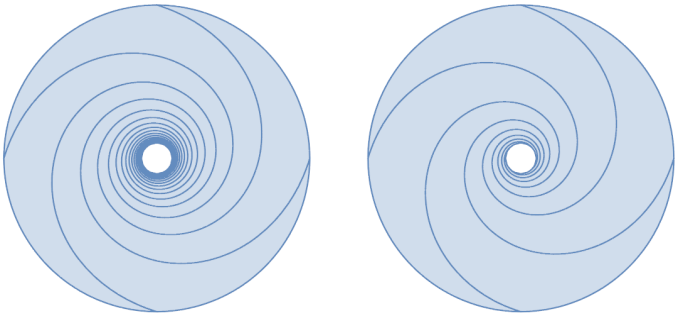

Fig. 13 Streamlines with low (left) and high (right) β-values

The length of the streamlines with high-β conditions is higher compared to the low-β case. Therefore, the fluid makes more revolutions, before it leaves the rotor. Higher β-values indicate higher friction and therefore a better turbine performance.

3.6 Compressibility effects onto rotor performance

At first it is shown, that the results of the flow model for the incompressible and the compressible flow agree very well for Mach numbers below 0.1 (see Fig. 14). In order to compare Fig. 14 and 15 well, torque and power are made dimensionless with the maximum values of the incompressible solution of Fig. 15.

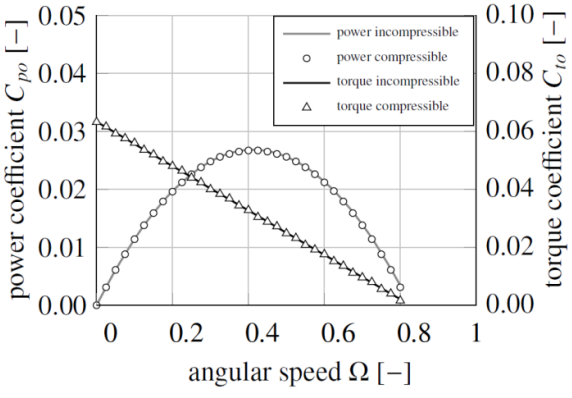

Fig. 14 Performance map with radial Mach number $Ma < 0.1$

Figure 15 indicates, that the deviation between the in-compressible and the compressible flow model expands more and more with increasing Mach number. Especially at high angular velocities, less power is delivered, because of com-pressibility effects. A closer look onto the trend of the radial velocity across the disk radius reveals that the divergence is rising constantly with the radial Mach number (Fig. 16). According to Eq. (13) and (14), higher outlet velocities lead to lower torque resp. to lower shaft power. For $Ma < 0.1$ both models return identical results, as physically expected.

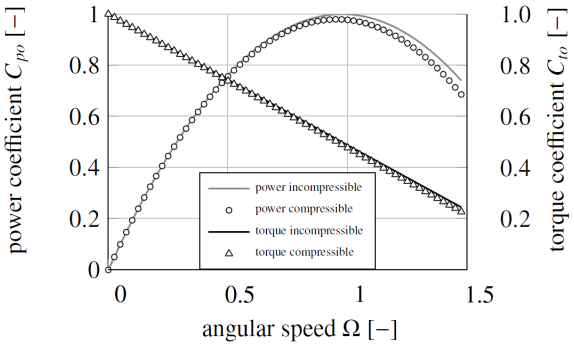

Fig. 15 Performance map with radial Mach number $Ma < 0.5$

Moreover, low β-values correspond to high Reynolds numbers.

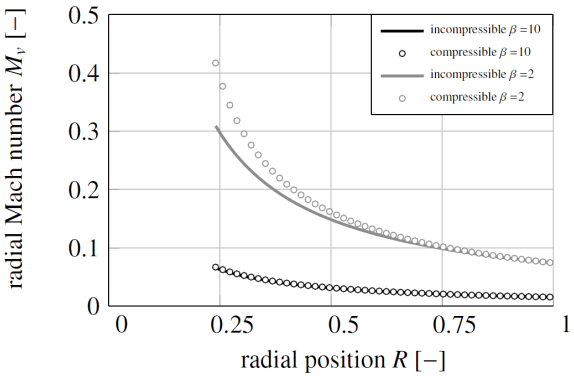

Fig. 16 Development of radial Mach number across the radius

4 Laminar CFD model analysis

In order to analyse the theoretical, incompressible, laminar turbine investigation, various laminar CFD RANS calculations are performed.

4.1 Mesh independency and CFD settings

The hexa mesh is designed with ICEM 14.5. ANSYS CFX 14.5 is used as a solver. To find a mesh independent solution, the grid has been refined until the outlet velocities had converged. A stationary mesh with co-rotating sidewalls and a rotating mesh show identical results. Rotating domain results are presented here.

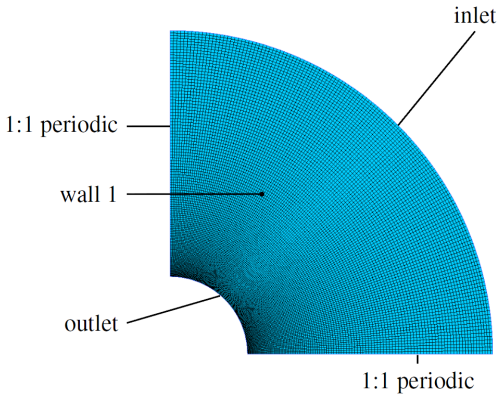

Fig. 17 Mesh, ¼ disk, 756000 nodes, view 1

The CFD settings for the calculation applied here are:

- geometry: r_1=125mm, r_2=30mm, gap width $2s$=0.2mm
- meshes: 224000, 540000, 756000, 1458000, 3400000 nodes (results from underlined mesh)
- rotating domain section (1:1 periodic interface)
- air at 25°C, laminar flow
- no turbulence model, no heat transfer
- inlet: velocity magnitude 105 m/s, variable V_1
- outlet: ambient pressure p_2 = 1 bar
- residual convergence: $1{\cdot}10^{-5}$ RMS, $1{\cdot}10^{-3}$ MAX
- auto timescale, double precision
- Ω is made dimensionless with u_1 = 100 m/s

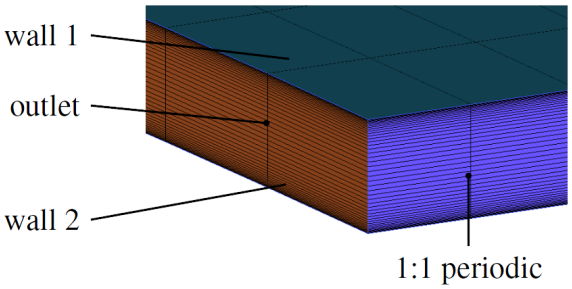

Fig. 18 Mesh, ¼ disk, 756000 nodes, view 2

4.2 Comparison of incompressible theory and CFD

This section reveals the limitations of the simplified incompressible model in a comparison with the full set of three-dimensional Navier-Stokes-Equations for laminar flow. In the laminar CFD, as well as in the theoretical model, the inlet velocity is kept constant. The inlet angle V_1 or α, hence the velocity components u_1 and v_1 are changed to see the impact on turbine performance. The significant difference between theory and CFD is, that CFD can simulate the development of the velocity profiles across the rotor. All continuous curves are analytical results, the symbols represent CFD results. The vertically dashed lines in Fig. 19, 20 and 21 denote the mechanical limits of the examined Tesla rotor. Figure 19 shows the performance map of a Tesla turbine over the whole range of valid angular velocities and investigated inlet conditions.

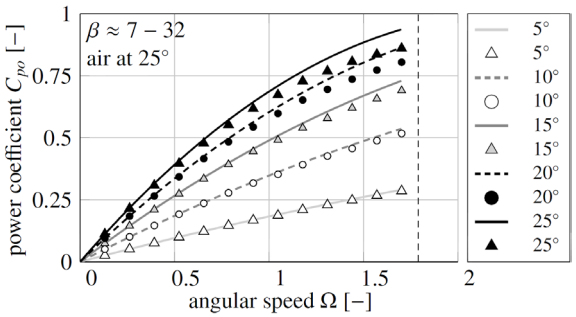

Fig. 19 Performance map comparison between CFD (marks) and analytical results (lines); vertical dashed line represents the mechanical limit

It can be observed, that there is a very good quantitative agreement between laminar CFD and analytical solution at low inlet angles. With increasing α and Ω, the solutions differ more and more from each other. The analytical solution over-predicts shaft power. Obviously, same applies to Fig. 20, where the torque map is plotted. Figure 21 illustrates the difference between both solutions regarding isentropic efficiency, where the deviation is at its worst. However, the qualitative agreement is satisfactory. To find the reasons for that, the velocity profile is examined in more detail in the next section. Figures 19, 20 and 21 confirm the results from theory. More power per gap leads to lower isentropic efficiencies - or vice versa.

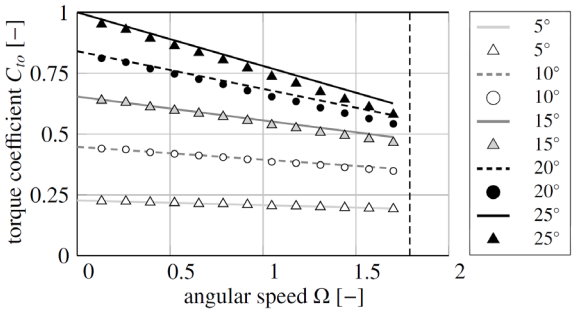

Fig. 20 Torque map comparison between CFD (marks) and analytical results (lines); vertical dashed line represents the mechanical limit

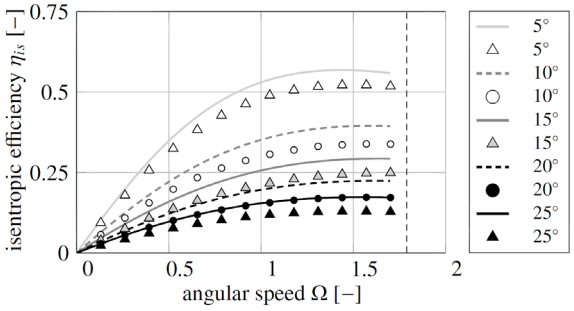

Fig. 21 Efficiency map comparison between CFD (marks) and analytical results (lines); vertical dashed line represents the mechanical limit

The inlet angle of about 15° and below is of technical importance for the application. The following sections are initiated to find explanations for the named deviations.

4.3 The inflow effect

The inflow effect on turbine performance is investigated by CFD to estimate errors of the theoretical model. In contrast to the expected profile development across the rotor, the model simply scales parabolic z velocity profiles with the bulk velocities $C(R)$, $V(R)$ to compute turbine performance from the resulting circumferential shear stress. In the first CFD setup, „block profile" approximations are selected at the rotor. Due to the gap between stator and rotor, this is expected to happen in real Tesla turbines. To quantify the fully developed flow, velocity profiles $F_n(R,Z)$ in circumferential and $G(R,Z)$ in radial direction are analysed.

$$C(R,Z) = U(R,Z) - R\cdot\Omega = \frac{V_1}{R}\cdot F(R,Z) \tag{30}$$

$$V(R,Z) = -\frac{V_1}{R}\cdot G(R,Z) \tag{31}$$

Furthermore, the continuity equation in radial direction requires

$$\int_0^1 G(R,Z)\,dZ = 1. \tag{32}$$

The function $F_n(R,Z)$ is normalised by dividing the profile F by its numerical integral

$$F_n(R,Z) = \frac{F(R,Z)}{\int_0^1 F(R,Z)\,dZ}. \tag{33}$$

Moreover, factorised solutions in circumferential

$$F_n(R,Z) = F_n(Z)\cdot C(R) \tag{34}$$

and radial direction

$$G(R,Z) = G(Z)\cdot V(R) \tag{35}$$

are sought. $F_n(R,Z)$ and $G(R,Z)$ are fully developed CFD profiles. Numerous CFD calculations were performed. As an example, the development of the velocity profiles in circumferential and radial direction of a typical operating point $\Omega = 0.92$, $V_1 = 0.27$ is shown in Fig. 22 and 23. The fully developed profiles $F_n(R,Z)$ and $G(R,Z)$ are used as new inlet profiles in a second CFD.

The performance and efficiency of both numerical computations and of the theoretical solutions are illustrated in Fig. 24 and 25.

At small inlet angles the results show very good agreement.

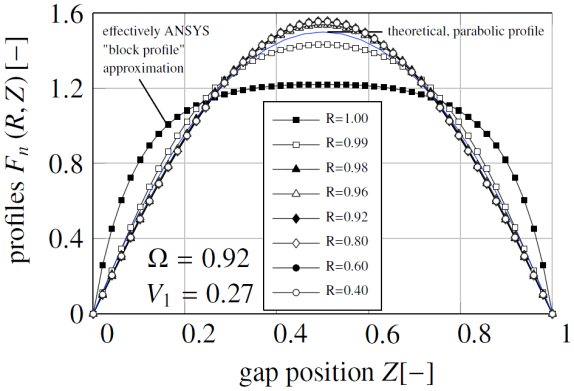

Fig. 22 Velocity profiles $F_n(R,Z)$

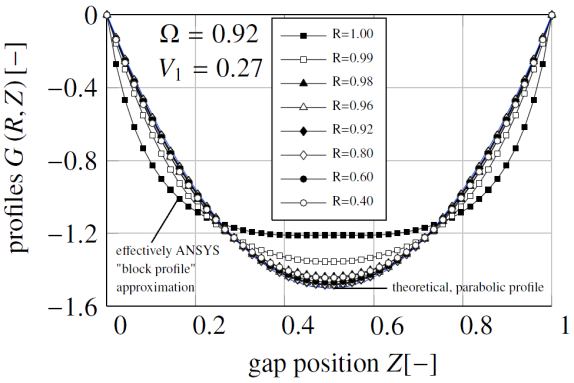

Fig. 23 Velocity profiles $G(R,Z)$

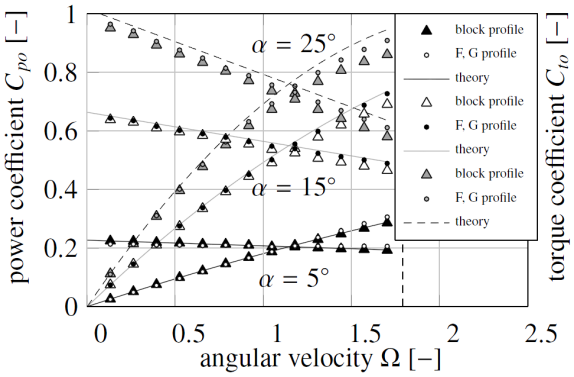

Fig. 24 Performance map comparison

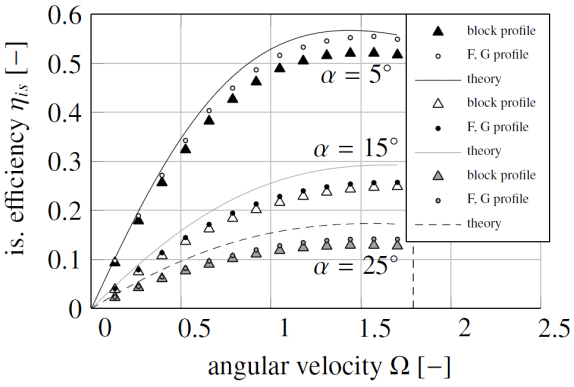

Fig. 25 Efficiency map comparison

With increasing inlet angles, the solutions slightly start to separate from each other. With increasing angular speed, the solutions begin to separate as well. The theory is generally overpredicting torque and power, the first CFD shows the lowest performance. In terms of efficiency, the trends of the presented solutions are similar, but the deviations are a bit higher. Theoretical results are overestimating isentropic rotor efficiency. Figure 26 shows the velocity distributions of both CFD calculations and of the theory. In general, the CFD results show higher velocity magnitudes compared to theoretical results. The block profile velocity magnitudes are slightly higher than those from the *F*, *G*-inlet profile CFD. In contrast to the results from the incompressible flow model, CFD shows higher pressure drops across the rotor (cf. Fig. 28).

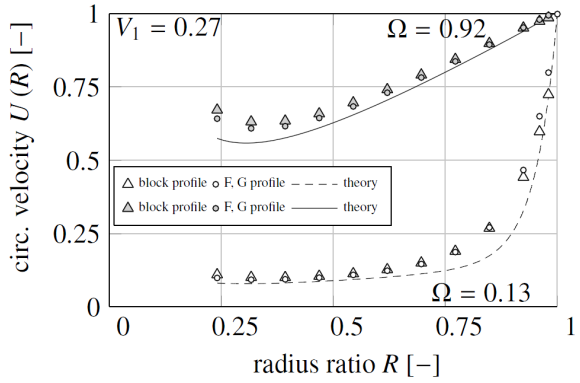

Fig. 26 Tangential, absolute bulk velocity comparison

The radial velocity distribution instead, show good agreement between CFD and theory (see Fig. 27 for details).

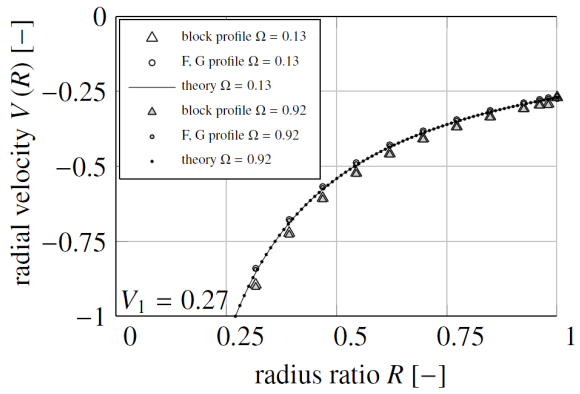

Fig. 27 Radial bulk velocity comparison

Nevertheless, the tangential velocity distribution is crucial for turbine performance. The deviations in isentropic efficiency (Fig. 25) are the result of the sum of the differences in the pressure drop and the differences in the tangential velocity distribution.

An interesting observation about the rotor flow in Tesla turbines is the radial development of the torque coefficient (Fig. 29). The block profile simulation generates a little more torque at high radius ratios. This can be explained by a higher tangen-tial wall shear stress at the inlet zone (Fig. 29). With decreasing radius ratio, the fully developed inflow simulation is gaining the upper hand again, now producing slightly more torque and power. This is valid for all simulated angular velocities. Obviously, block profiles' higher wall shear stress in radial direction leads to a higher pressure drop. As the outlet pressure is kept constant, the inlet pressure must increase. This makes the flow marginally faster towards the outlet. Hence, the block profiled inflow produces less total torque and power. Dependent on the angular velocity, shaft power differs by up to 5% in this case. The differences in torque and pressure drop between theory and CFD, explain the difference in isentropic efficiency of up to 10% (see Fig. 25). The difference between theoretical analysis and CFD are depending on the selected values of V_1 and Ω. They cannot fully be attributed to the inflow effect.

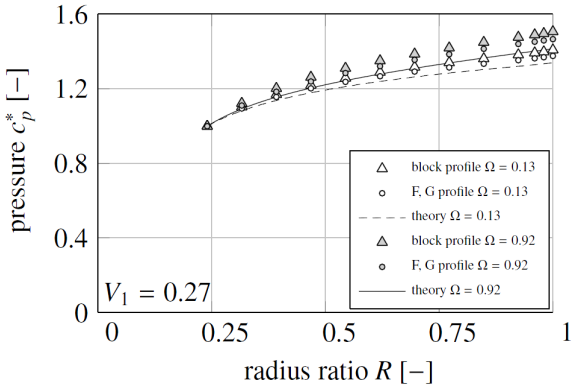

Fig. 28 Pressure drop across the rotor radius

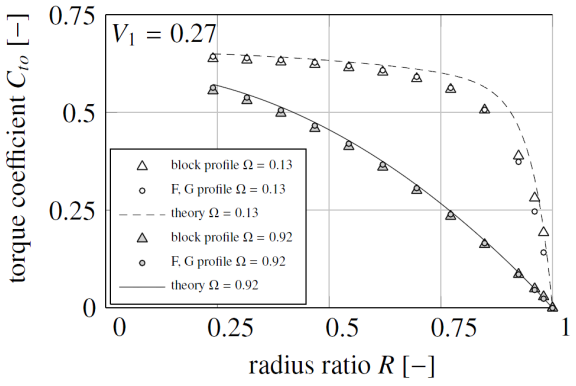

Fig. 29 Torque coefficient comparison

4.4 Influence of Reynolds number on velocity profile

Figures 22 and 23 show examples of the development of the axial velocity distribution of a „block profile" inflow as a function of the radius. The fully developed velocity profiles were fitted by a fourth-order polynomial for the whole range of typical Reynolds numbers. These fits are illustrated in Fig. 30 and 31. Neither in radial, nor in tangential direction, any dependency of the Reynolds number on the fully developed velocity profiles is detectable.

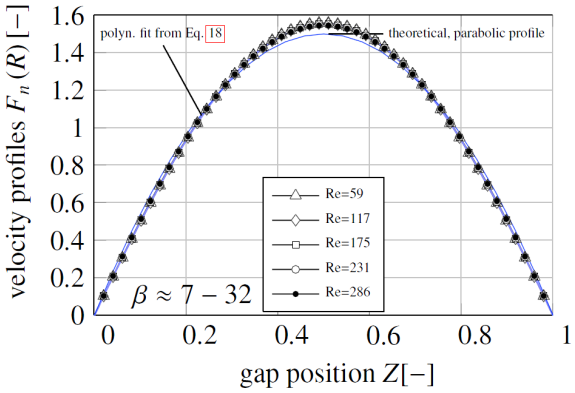

Fig. 30 Fully developed velocity profiles $F_n(R)$

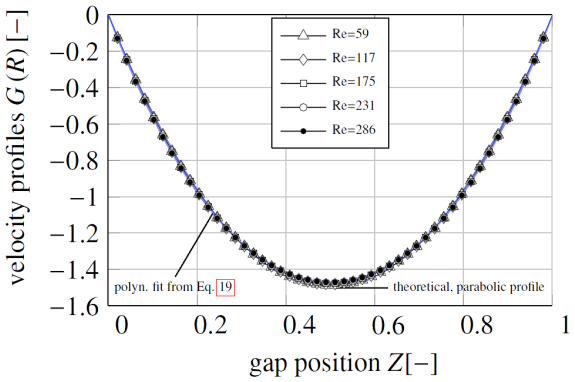

Fig. 31 Fully developed velocity profiles $G(R)$

4.5 Influence of revolution speed on velocity profile

The fully developed velocity profiles are determined from the laminar CFD. They depend only weakly on revolution speed. The radial velocity profile $G(Z)$ approximates the parabolic profile quite well. Instead, the circumferential or tangential velocity distribution $F_n(Z)$ deviates from the original assumption of a parabolic velocity profile and influences the momentum transfer from fluid to wall. Fourth order polynomials are preferable for a mathematical description of the axial velocity distribution. Obviously, this has a small impact on the model prediction of torque and shaft power.

4.6 Axial velocity distribution

Several Tesla rotor flow models like the ones presented in [3, 7, 9], as well as the models described before [1] assume that the third velocity component is zero compared to the radial and tangential velocity distribution. The axial velocity distribution over the inter-disk spacing for different radial positions are shown in Fig. 32. The results come from the laminar CFD, described in Section 4.1. The axial velocity is non-dimensionalised with the inlet velocity from the outlet of the guide vanes. Considering the velocity magnitudes, it seems that the assumptions underlying most theoretical description of those flows are correct. The axial velocities show maxima near the wall. Nevertheless, it is surprising, that the peaks are in the same order of magnitude for all examined revolution speeds. With decreasing radius ratio, the velocities maxima are constantly reduced.

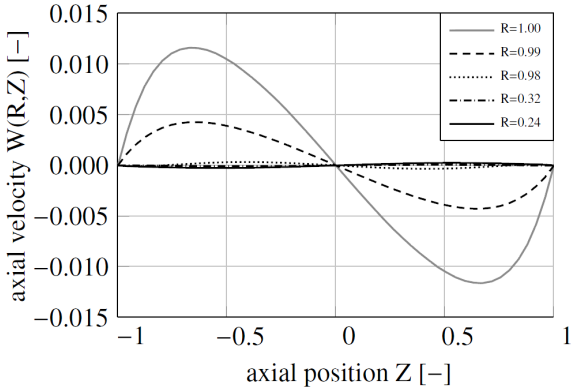

Fig. 32 Axial velocity component $W(R,Z)$

5 Concluding remarks

To simplify the process of designing a Tesla turbine, the flow analysis is coupled with the analytical equation for tangential stress in centrally, drilled and rotating disks. This exposes the maximum applicable angular speed from mechanical integrity considerations.

Furthermore, the influence of the dimensionless machine parameters on shaft power and isentropic efficiency are derived. The typical operational behaviour of a Tesla turbine is shown. As a consequence of these discrepancies, the best compromise between high efficiency and shaft power per gap is figured out.

In addition to that the incompressible flow model is extended to compressible flow conditions. Therefore, the governing equations are only coupled solvable by numerical means. Nevertheless, this offers the exploration of compressibility effects. The model is validated with a comparison to the incompressible model, where it is shown, that both models behave similar under incompressible flow conditions.

Streamlines of the bulk flow are visualised. An analytical function is found. The development of the streamlines are related to the expected turbine performance and agrees well with the existing theoretical knowledge about Tesla rotors.

Moreover, various analytical results from theory are analysed and so to say validated by laminar CFD. The accuracy limitations of the theoretical analysis are explained. At higher inlet angles, the theoretical solution deviates more and more from the laminar CFD. Torque and power are up to 5% higher, isentropic efficiency is about 10% lower. The qualitative agreement instead, is very promising.

In search of reasons for that, an investigation of the development of the velocity profiles and their influence on shaft power and efficiency is performed by means of CFD. Fully developed profiles at the rotor inlet lead to higher predicted shaft power. This and the fact that CFD produces higher pressure drops, explain the deviations in efficiency. Nevertheless, the inflow effect is only a partial explanation. The difference increases with the parameters α resp. V_1 and Ω.

The mathematical character of the velocity distribution between the disks is found for a typical range of Reynolds

numbers. The main difference between theory and laminar CFD is, that the CFD profiles in both directions are not fully parabolic and can best be approximated by fourth-order polynomial functions. However, the assumption of the parabolic velocity distribution in radial direction is closer to CFD than expected.

Despite certain differences to the CFD, the theoretical model is a very fast tool for dimensioning rotors. Applying suitable corrections, the accuracy of this method can be improved in the future.

Acknowledgement

This work is supported by the Faculty of Mechanical Engineering of the Bundeswehr University in Munich.

References

[1] Schosser, C., Lecheler, S., Pfitzner, M. "A test rig for the investigation of the performance and flow field of Tesla friction turbines." Paper No.: GT2014-25399, In: ASME Turbo Expo 2014: Turbine Technical Conference and Exposition, Dusseldorf, Germany, June 16-20, 2014. pp. V01BT24A009. https://doi.org/10.1115/GT2014-25399

[2] Tesla, N. "Tesla turbine." US Patent 1061206 A, 1913. URL: http://www.google.com/patents/US1061206

[3] Romanin, V. D. "Theory and Performance of Tesla Turbines." PhD. Thesis, University of California, Berkley. 2012. URL: http://escholarship.org/uc/item/6584x24x#page-2

[4] Romanin, V. D., Krishnan, V. G., Carey, V. P., Maharabiz, M. M. "Experimental and analytical study of sub-watt scale Tesla Turbine performance." Paper No.: IMECE2012-89675. In: ASME 2012 International Mechanical Engineering Congress and Exposition, Houston, Texas, Nov. 9-15, 2012. pp. 1005-1014. https://doi.org/10.1115/IMECE2012-89675

[5] Krishnan, V. G., Romanin, V., Carey, V. P., Maharabiz, M. M. "Design and scaling of microscale Tesla Turbines." *Journal of Micromechanics and Microengineering*. 23(12), Article No.:125001. https://doi.org/10.1088/0960-1317/23/12/125001

[6] Rice, W. "An analytical and experimental investigation of multiple-disk turbines." *Journal of Engineering and Power*. 87(1), pp. 29-36. 1965. https://doi.org/10.1115/1.3678134

[7] Guha, A., Sengupta, S. "The fluid dynamics of work transfer in the non-uniform viscous rotating flow within a Tesla disc turbomachine." *Physics of Fluids*. 26(3), Paper No.:033601. 2014. https://doi.org/10.1063/1.4866263

[8] Guha, A., Sengupta, S. "Similitude and scaling laws for the rotating flow between concentric discs." *Journal of Power and Energy*. 228(4), pp. 429-439. 2014. https://doi.org/10.1177/0957650914523947

[9] Romanin, V. D., Carey, V. P. "An integral perturbation model of flow and momentum transport in rotating microchannels with smooth or microstructured wall surfaces." *Physics of Fluids*. 23, Article No.: 082003. 2011. https://doi.org/10.1063/1.3624599

[10] Schosser, C., Pfitzner, M. "A numerical study of the three-dimensional incompressible rotor airflow within a Tesla turbine." In: Conference of Modelling Fluid Flow CMFF'2015, Budapest, Hungary, Sept 1-4, 2015.

[11] Schosser, C., Hain, R., Cierpka, C., Lecheler, S., Kähler, C. J., Pfitzner, M. "Determination of velocity profiles in small gaps between parallel flat plates by means of tomographic PIV." In: 21. FachtagungLasermethoden der Strömungs-messtechnik 2013, Munich, Germany, Sept. 3-5, 2013. pp. 1-8. URL: http://www.gala-ev.org/images/Beitraege/Beitraege%202013/pdf/15.pdf

[12] Beans, E. W. "Performance characteristics of a friction disc turbine." PhD Thesis, Pennsylvania State University. 1961.

[13] Beans, E. W. "Investigations into the performance characteristics of a friction turbine." *Journal of Spacecraft and Rockets*. 3(1), pp. 131-134. 1966. https://doi.org/10.2514/3.28398

[14] Davies, B. J., Beitz, W., Kuttner, K.-H. "*DUBBEL - Handbook of Mechanical Engineering*." Springer, 1994. https://doi.org/10.1007/978-1-4471-3566-1